In-depth study of the formation processes of single atmospheric particles in the southeastern margin of Tibetan Plateau

Li Li[1,3], Qiyuan Wang[1,2,3], Jie Tian[1], Huikun Liu[1], Yong Zhang[1], Steven Sai Hang Ho[4], Weikang Ran[1], Junji Cao[5]

[1] Key Laboratory of Aerosol Chemistry and Physics, State Key Laboratory of Loess and Quaternary Geology, Institute of Earth Environment, Chinese Academy of Sciences, Xi'an 710061, China

[2] CAS Center for Excellence in Quaternary Science and Global Change, Xi'an 710061, China

[3] University of Chinese Academy of Sciences, Beijing 100049, China

[4] Division of Atmospheric Sciences, Desert Research Institute, Reno, NV 89512, United States

[5] Institute of Atmospheric Physics, Chinese Academy of Sciences, Beijing 100029, China

Correspondence to: Qiyuan Wang (wangqy@ieecas.cn) and Junji Cao (jjcao@mail.iap.ac.cn).

Abstract

The unique geographical location of the Tibetan Plateau (TP) plays an important role in regulating global climate change, but the impacts of the chemical components and atmospheric processing on the size distribution and mixing state of individual particles are rarely explored in the southeastern margin of the TP, which is a transport channel for pollutants from Southeast Asia to the TP during the pre-monsoon season. Thus a single-particle aerosol mass spectrometer (SPAMS) was deployed to investigate how the local emissions of chemical composition interact with the transporting particles and assess the mixing state of different particle types and secondary formation in this study. The TP particles were classified into six distinct types, mainly including the largest fraction of the rich-potassium (rich-K) type in the total particles (30.9%), followed by the biomass burning (BB) type (18.7%). Most particle types were mainly transported from surroundings the sampling site and along the Sino-Myanmar border; but the air mass trajectories from northeastern India and Myanmar show a greater impact on the number fraction of BB (31.7%) and Dust (18.2%) types, respectively. Then, the two episodes with high particle concentrations showed that the differences in the meteorological conditions in the same trajectory clusters could cause significant changes in chemical components, especially the Dust and EC-aged types, which changed by a sum of 93.6% and 72.0%, respectively. Ammonium and Dust particles distribute at a relatively larger size ($\sim$ 600 nm), but the size peak of other types is present at $\sim$ 440 nm. Compared with the abundant sulfate ($^{97}HSO_4^-$), the low nitrate ($^{62}NO_3^-$) internally mixed in TP particles is mainly due to the fact that nitrate is more volatilized during the transport process. The formation mechanism of secondary speciation demonstrate that the formation capacity of atmospheric oxidation is presumably affected by the convective transmission and the regional transport in TP. However, the relative humidity (RH) could significantly promote the formation of secondary species, especially $^{97}HSO_4^-$ and $^{18}NH_4^+$. This study provides new insights into the particle composition and size, mixing state, and aging mechanism in high time resolution over the TP region.

Keywords

Southeastern Tibetan Plateau, Individual particles, Chemical characteristics, mixing state,

44   Secondary formation

1 Introduction

46   Atmospheric aerosols have complex components and sources and can be coated with

47   inorganic or organic materials during transport and atmospheric processing (Crippa et al.,

48   2013), and then its sizes, chemical compositions, mixing states and optical properties would

49   change greatly, leading to its influence in the atmosphere more uncertain (Jacobson, 2002;

50   Zaveri et al., 2010; Matsui, 2016; Budisulistiorini et al., 2017; Ma et al., 2012). Currently, the

51   influences of the complex chemical components on aerosol size and mixing state show large

52   regional differences due to the variations in the pollution sources, atmospheric formation

53   mechanism and meteorological conditions, which have been widely studied in an urban area

54   at a low altitude (Pratt et al., 2011; Liu et al., 2020a; Xu et al., 2017; Wang et al., 2022).

55   However, Liu et al (2020) have found that the migration or formation of low-volatile

56   component (such as nitrate and organic matter) could effectively be reduced due to

57   evaporation during the upward transportation process, which further alter the chemical

58   compositions and the particle sizes. The transportation of the aerosols to a relatively cleaner

59   environment prevails the formation of secondary chemicals at a high altitude (Liu et al.,

60   2020b). Therefore, a comprehensive investigation of the detailed characteristic of aerosol

61   formation and mixing states is required to understand their environmental effects in low-, and

62   high-altitude.

63   As a typical high-altitude region, the Tibetan Plateau (TP) has the highest and largest

64   mountain area in the world, which is the most sensitive and obvious indicator of climate

65   change in the entire Asian continent (Liu et al., 2017; Chen and Bordoni, 2014; Immerzeel et

66   al., 2010). Numerous studies have shown that the melting and retreat of glaciers in the TP

67   regions is accelerating in recent decades, largely attributed to anthropogenic emissions, such

68   as greenhouse gases and aerosols (Luo et al., 2020; Hua et al., 2019). Atmospheric aerosols

69   also can act as cloud condensation nuclei to impact the local hydrological cycles and

70   monsoon patterns by changing the microphysical properties and life span of clouds (Qian et

71   al., 2011; Gettelman et al., 2013; Kumar et al., 2017). The southern part of the TP is always

72   affected by the transport of more polluted air from South Asia along the mountain valleys,

73 especially during the pre-monsoon (i.e., March-May) with the southwest prevailing wind
74 (Chan et al., 2017; Zhao et al., 2017; Han et al., 2020). Most studies have focused on the
75 optical characteristics within the TP; however, only a few research has been conducted on
76 aerosol components.

77 Present researches on aerosol components over the TP mostly focus on exploring the
78 influence of light-absorbing carbon aerosols and dust particles on climate change by optical
79 or offline sampling methods (e.g., Wang et al., 2019a; Liu et al., 2021). There is a lack of
80 studies on the chemical composition, mixing states, and formation mechanism of aerosols in
81 the southeast margin and even the entire TP, especially using high-time resolved
82 measurements. Although time-integrated sampling with filter collection followed by
83 laboratory analyses has been widely adopted for the chemical characterization of aerosols (Li
84 et al., 2022a; Shen et al., 2015; Zhang et al., 2013), the drawbacks of the traditional approach
85 need to get attention, including the low time resolution, high detection limit, and time- and
86 labor-intensive procedures. Therefore, more advanced aerosol measurement equipment with
87 high-time resolution are developed, for example the aerosol chemical speciation monitor
88 (ACSM) and aerosol mass spectrometer (AMS) (Ng et al., 2011; Canagaratna et al., 2007) are
89 mainly achieved the online observation datasets of non-refractory submicron aerosol
90 (including the mass concentration of sulfate, nitrate, ammonium, chloride and organic; and
91 mass spectral of organic). This is beneficial to recognize the dynamic processes of source
92 emission of organic matter in the atmosphere (Du et al., 2015; Zhang et al., 2019a).
93 Meanwhile, aerosol time-of-flight mass spectrometry (ATOFMS) (Dall'Osto et al., 2014) and
94 single particle aerosol mass spectrometer (SPAMS) (Zhang et al., 2020) are popular for
95 characterizing atmospheric individual particles. These devices can determine the chemical
96 composition and size distribution of the particles in detail, such as the dynamic processes of
97 chemical aging, mixing state and transporting (Liang et al., 2022; Li et al., 2022b; Zhang et
98 al., 2019b). To the best knowledge, the advanced measurement device has not yet been
99 applied for the studies conducted in TP, leading to a lack of in-depth research on the $PM_{2.5}$
100 pollution in TP, especially in the southeastern margin, which hinders our understanding of the
101 distribution characteristics and formation mechanism of aerosol components in high-altitude
102 regions.

103   The southeastern margin of the TP is an important transitional zone between the
104   high-altitude TP and the low-altitude Yungui Plateau (Wang et al., 2019a; Zhao et al., 2017),
105   is an ideal place for investigating the impacts of pollutants transport and formation in the
106   high-altitude zone. In this study, continuous field observation of individual particles (SPAMS)
107   was deployed on the southeastern margin of the TP during the pre-monsoon period, to (i)
108   investigate the changes of chemical characteristics between transport and local fine particles
109   during pre-monsoon, (ii) determine the size distributions and mixing states of different
110   particle types, and (iii) assess the contributions of photooxidation and aqueous reaction to the
111   formation of the secondary species. These results would expand our understanding of the
112   chemical components, size distribution, mixing state and aging pathways of aerosols in the
113   high-altitude areas over the TP and surrounding areas.

114 **2 Methodology**

115 **2.1 Sampling site**

116   Intensive one-month field observation was deployed at the rooftop ($\sim$ 10 m above ground
117   level) of the Lijiang Astronomical Station, Chinese Academy of Sciences (3260 m above sea
118   level; 26°41′24″N, 100°10′48″E), Gaomeigu County, Yunnan Province, China, during the
119   pre-monsoon period (from April 14th to May 13th, 2018). The nearest residential area is the
120   Gaomeigu village (3–5 km away) with a small population size of 113 residents in 27
121   households. Villagers earn a living by farming (e.g., potato and autumn rape), and biomass is
122   the major domestic fuel (Li et al., 2016). The sampling site is surrounded by rural and
123   mountainous areas and has no obvious industry or traffic emissions. During the total
124   observation period, the average temperature (T) and relative humidity (RH) are 8.4 ± 3.1°C
125   and 69% ± 21%, respectively. The wind speed (WS) is 2.2 ± 1.2 m·s^{-1} with the prevailing
126   wind in the north and northeastern (Fig. S1).

127 **2.2 On-line instrument**

128   A detailed operational principle and the calibrations of the single-particle aerosol mass
129   spectrometer (SPAMS, Hexin Analytical Instrument Co., Ltd., Guangzhou, China) has been
130   described elsewhere (Li et al., 2011). Briefly, individual particles are drawn into SPAMS

through a critical orifice. The particles are focused and accelerated, then aerodynamically sized by two continuous diode Nd: YAG laser beams (532 nm), subsequently desorbed and ionized by a pulsed laser (266 nm) triggered exactly based on the velocity of the specific particle. The generated of positive and negative molecular fragments are recorded with the corresponding size of individual particles. In summary, a velocity, a detection time, and an ion mass spectrum are recorded for each ionized particle, while there is no mass spectrum for not ionized particles. The velocity could be converted to d_{va} based on a calibration using polystyrene latex spheres (PSL, Thermo Scientific Corp., Palo Alto, USA) with predefined sizes. The average ambient pressure is 690 hPa (in a range of 685–694 hPa) during the measurements and calibration. A hollow silicone dryer was installed in front of the inlet. This reduces the uncertainty of particle collection efficiency due to the changes of humidity in sampled airs. Particles measured by SPAMS mostly are within the size range of vacuum aerodynamic diameter (d_{va}) 0.2–2.0 μm. This SPAMS-specific size distribution is semi-quantitative evaluated the relative concentration and contribution of each particle type, mainly due to it largely dependence on the particle-detection efficiency (Allen et al., 2000; Yang et al., 2017). The characteristics of SPAMS-specific size distribution are statistical results, while the comparison of the relative distribution and number fraction of different particle types in each size bin are significant.

Meteorological parameters, including the temperature (°C), RH (%), WS (m·s^{-1}), and wind direction (WD) were continuously achieved using an automatic weather station (Model MAWS201, Vaisala HydroMet, Helsinki, Finland) in a 5-min resolution, and the planetary boundary layer (PBL) was acquired from the website (https://rda.ucar.edu/datasets/ds083.2, last access: 17 April 2020) in a 1-hour resolution. Gaseous concentrations (ppbv) were obtained using a multiple gas analyzer (Thermo Scientific Corp.), including ozone (O$_3$, model 49i) and nitrogen oxides (NO$_x$, model 42i) in a 5-min resolution. The SPAMS and gas analyzers are co-located in the same position, and the weather station was uncovered outside ~5 m from the sampling house. Time series of SPAMS particles, gaseous concentrations (NO, NO$_x$, O$_3$, and CO) and meteorological parameters (PBL, temperature, RH, WD, and WS) were shown in Fig. S2.

2.3 Individual particle classification

During the observation period, a total of 461,876 ambient particles with the size (d_{va}) of 0.2–2.0 μm were collected, including 55,583 in Episode 1 (E1; from April 18th 08:00 local time (LT) to April 19th 08:00 LT) and 62,110 in Episode 2 (E2; from April 26th 17:00 LT to April 28th 02:00 LT). The analyzed particles are classified into 1,557 groups using an adaptive resonance theory neural network (ART-2a) with a vigilance factor of 0.8, a learning rate of 0.05, and 20 iterations (Song et al., 1999). Finally, eight major particle clusters [i.e., potassium-rich (rich-K), biomass burning (BB), organic carbon (OC), Ammonium, aged element carbon (EC-aged), Dust, sodium (Na)-potassium (K)-containing (NaK-SN), and iron (Fe)-lead (Pb)-containing (Metal)] with distinct chemical patterns were manually combined, which represent ∼99.7 % of the population of the detected particles. The remaining particles are grouped as "Other". The characteristics of the positive and negative mass spectra (MS) of each particle type are shown in Fig. S3. A detailed description of classification criteria for individual particles and the characteristic ion fragments for each particle type can be found in Text S1. The criteria used for searching the some secondary species in the SPAMS datasets are summarized in Table S2.

2.4 Trajectory-related analysis

To determine the influence of regional transport on different particles at the southeastern margin of the TP, the trajectory clusters analysis was carried out using the 72-h backward air mass trajectories at arrival heights of 500 m above ground level. The trajectories were calculated with the Hybrid Single-Particle Lagrangian Integrated Trajectory model (Draxler and Hess, 1998), and the meteorological data were obtained from the Global Data Assimilation System (GDAS; ftp://arlftp.arlhq.noaa.gov/pub/archives/gdas1, last access: 6 April, 2022). The cluster analysis employs a Euclidean-oriented distance definition to differentiate and cluster the major spatial features of the inputting trajectories. Details of the trajectory clustering method can be found in Sirois and Bottenheim (1995). To investigate the effects of transport on the chemical characteristic of the individual particles, trajectories with particle number concentrations high than the 75th percentile are considered as pollution (Liu et al., 2021).

3 Results and Discussion

3.1 Characteristics of particle composition

Table 1 summarizes the number concentrations, relative percentages and characteristic ions of each particle type. The most dominant particle type in Gaomeigu during pre-monsoon is rich-K, accounting for an average of 30.9% of the total resolved particles, followed by BB (18.7%), OC (12.8%), Ammonium (11.9%), EC-aged (10.9%) and Dust (10.7%). Their characteristics of mass spectrum and possible sources are described in supplemental information of text S1 in detail. Similar to the results of some studies in urban areas, rich-K or carbonaceous-containing type is the dominant particle type (15-50%) (Xu et al., 2018; Wang et al., 2019b; Li et al., 2022). Combined with the previous studies and the characteristics of the mass spectrum (Fig. S3a) in this study, the rich-K particles are contributed by biomass burning and traffic emission, because that extensive works usually identify abundant $^{39}K^+$ signals for biomass burning (Pratt et al., 2011; Chen et al., 2017), while the presence of phosphate (m/z $^{79}PO_3^-$) indicates the vehicle exhaust (Yang et al., 2017). The results of the correlation between seven variables (Fig. S4) show that rich-K type is strongly correlated with Ammonium (r=0.84) and EC-aged (r=0.90) types, follow well correlated with OC (r=0.70) and BB (r=0.68) types, further demonstrate that rich-K particles type is from traffic emission and biomass burning, and is affected by secondary formation during the atmospheric aging in southeastern TP. It is worth noting that few research have captured the high proportion of Ammonium particles as shown in this study (Shen et al., 2017; Xu et al., 2018), which is ascribed to the conversion of ammonia (NH_3) precursor emitted from large-scale agricultural activities and mountain forest (Engling et al., 2011; Li et al., 2013). It is necessary to point out that 60% of Ammonium particles contain signals of amine fragment (m/z 58, $C_2H_5NH=CH_2^+$), implying their similar formation pathway (Zhang et al., 2012). Moreover, the amine-containing particle represented 12.5% of the total ambient particles, which is significantly higher than that in some urban areas at low altitudes (around 2%) (Cahi et al., 2012; Zhang et al., 2015; Li et al., 2017) but is comparable to that at observed sites with high RH, or during fog and cloud events at a high altitude (> 9%) (Roth et al., 2016; Lin et al., 2019). This suggests that the formation of amines under high RH and fog

conditions might exist in the Gaomeigu area (with an altitude of 3260 m), for example, the high relative fraction of amine-containing particle corresponds to a high RH (Fig. S5), and the existence of amine sources govern the ammonium formations (Bi et al., 2016; Rehbein et al., 2011). The relatively larger fraction of Dust particles is related to the short-time occurrences of dust events in spring (Fig. S6), leading to a wide contribution ranging between 10% and 70% in the period of 19:00 LT on April 16th to 10:00 LT on April 17th.

Fig. 1 shows the diurnal variations of each particle type. The rich-K, BB and OC particles decrease after midnight until 06:00 LT, possibly explained by the curtailment of local traffic and biomass-burning activities at nighttime even though both the planetary boundary layer (PBL) height and WS decrease (Fig. S7). Then, their concentrations rapidly increase in the morning (around 07:00 LT) due to more pollutants from biomass burning and traffic emissions at the upwind region. The increases of PBL height and WS also lead to the transported of air pollutants from the surrounding regions to the sampling site (Liu et al., 2021). At 11:00 LT, the particle concentrations sharply decrease till 16:00–17:00 LT, caused by the pollutant dispersion with the continuing increases of the PBL height and WS. Increasing trends are observed after 17:00 LT due to the pollutant accumulation with the reduction of PBL height and WS. In contrast, the Ammonium, EC-aged and Dust particles show a unimodal pattern of the daily diurnal variation (Fig. 1d–f). From 00:00 to 06:00 LT, minor fluctuation of particle concentrations of Ammonium, EC-aged and Dust is observed for these particle types. After that, their levels continuously elevate until ~11:00 LT due to the regional transport, traffic emission and fugitive dust (Text S2). While the PBL height and WS increase continuously, the Ammonium, EC-aged and Dust types begin to decline from 12:00 to 17:00 LT. The subsequent increases of these three types after 17:00 LT are attributed to the reduction of PBL height, as a result of the accumulation of pollutants in the near-surface atmosphere.

Based on the transport pathways, four air mass clusters are identified to investigate the effect of regional transport on the major particle types (i.e., rich-K, BB, OC, Ammonium, EC-aged and Dust) (Fig. 2). Cluster 1, 3 and 4 are originated from northeastern Myanmar, accounting for 59.8%, 33.2% and 4.6% of the total trajectories, respectively. Cluster 1 had an

average percentage of 32.7%, 18.5%, 12.0%, 12.5%, 11.1% and 8.9%, respectively, on the rich-K, BB, OC, Ammonium, EC-aged and Dust particles (Table S1). Cluster 3 and 4 have the comparable contributions of OC (15.5% and 12.5%, *respectively*), increased of BB (19.3% and 26.8%, *respectively*) and decreased of rich-K (26.8% and 25.2%, *respectively*), Ammonium (10.4% and 7.7%, *respectively*) and EC-aged (7.7% and 6.3%, *respectively*), to those of Cluster 1, but with a high contribution of Dust (16.6%), which refer Cluster 3 and 4 to as dust and biomass burning pollution. However, Cluster 1 is more influenced by compound pollution, mainly including secondary formation, biomass burning, and traffic emissions. The diurnal variations of the BB and OC fractions are similar which rapidly elevate at 07:00 LT (Fig. S8) due to the increased contribution of biomass burning and traffic emissions from Cluster 1, Ammonium and EC-aged particles (peak at 07:00 LT) caused by the effect of Cluster 1 and 3 together. A stable diurnal variation of rich-K fraction is mainly due to its large proportion and diverse sources. The similar diurnal trend of Clusters 3 and 4 are both associated with dust contributions, which decrease at 04:00 LT and increase at noon. The increased nighttime particles could be attributed to the pollutant accumulation with the decreased PBL height. Cluster 2 originate from the northeastern India and passes over Bangladesh. This cluster accounts for only 2.4 % of the total trajectories, in which ~30.8% and ~35.9% are mainly associated with the rich-K and BB particles, respectively. Although Cluster 2 and 4 are composed of a small fraction of total trajectories (2.4% and 4.6 %, respectively), BB and dust particles are identified as the major pollutants, suggesting significant influences from India and northeastern Myanmar during the campaign.

A more in-depth investigation of the characteristics of the main particle types in the southeastern Tibet Plateau was conducted during two episode periods when the number concentration of particles was high (i.e., E1: from 08:00 LT April 18th to 08:00 LT April 19th, 2018; E2: 17:00 LT April 26th to 02:00 LT April 28th, 2018) (Fig. S6). Even though the two episodes are contributed by Cluster 1, the chemical components show significant differences (Table 1). During E1, the average fractions of the rich-K, BB, OC, Ammonium, EC-aged, and Dust particle are 29.0%, 11.5%, 8.1%, 17.5%, 10.0% and 20.3%, respectively, different from 39.3%, 14.2%, 10.0%, 13.5%, 17.2%, and 1.3% respectively, during E2. It can be seen that

the major changed factor of the Dust particle is 93.6% lower during E2 than E1, whereas the EC-aged particle shows a reversible of 72.0% higher during E2. Meanwhile, rich-K, BB and OC particles also increase by 35.5%, 23.5% and 23.4% respectively during E1 compared to E2. For the air mass clusters (Fig. S9), E1 and E2 exhibit minor differences, mostly originating from northern Myanmar and the Sino-Burmese border, but not identical regions. The Dust particles that are much lower during E2 than E1 could be explained by higher WS (on average of 2.7 ± 1.0 m/s versus 0.4 ± 0.5 m/s) (Fig. S9) and PBL height (771 ± 717 m versus 560 ± 549 m) (Fig. S10). The Dust particles are mainly formed by re-suspension in the local areas. In addition, the quick thrown-up dust belongs to more coarse size particles, which are out of the detection range of the SPAMS. However, due to the larger dust particles deposited more easily under the low WS and the stagnant air conditions during E1, more suspended dust particles of small size fall in the detection range of SPAMS. Moreover, the increased PBL height and WS could speed up the transportation of pollutants from multiple sources (e.g., traffic and biomass burning emissions) to the observation site, leading to elevate the fraction of EC-aged, rich-K, BB, and OC particles during E2. The decreased Ammonium fraction during E2 is potentially explained by the reductions in the secondary pollutant formation with declines of RH (from $73.9\% \pm 23.9\%$ to $53.1\% \pm 14.9\%$), in comparison to those during E1.

3.2 Characteristics of SPAMS-specific size distribution and mixing state

The SPAMS-specific size distributions of all particle types are shown in Fig. 3. According to the characteristics of the average MS (Text S1 and Fig. S3), rich-K, BB, OC and EC-aged particles originated from the similar sources of solid-fuel combustion or vehicle emission. Their SPAMS-specific size distribution thus presents within a small-scale (~440 nm) (Fig. S11a). However, the relative percentage of each particle type is distinct with different size ranges, possibly due to the unique atmospheric processing. For example, as shown in Fig. 3a, the proportions of rich-K and BB types increases along with the increase in particle size from 200 to 420 nm, then decrease. OC and EC-aged types are mainly distributed in relatively small sizes, and their proportions gradually decrease when the size ranges become lager. Ammonium and Dust types are mainly distributed in large sizes of ~600 nm (Fig. S11a).

305   The proportion of Ammonium particles gradually increases with the increase of particle size

306   and peaks at 740 nm, the relatively large SPAMS-specific size distribution is ascribed to the

307   intense atmospheric aging during regional transport (Text S1). The proportion of Dust

308   particles gradually increases with a size > 560 nm and peaks at 1.48 μm. This is consistent

309   with the fact that dust is a coarse particle, generally formed at the roadside and fly ash.

310   Compared with the SPAMS-specific size distribution of the total particles, the peak

311   values of the six main particle types show minor differences (< 80 nm) during the two

312   different episode periods (Fig. 11b,c). However, the percentage of the six particle types

313   distribute in wider size ranges during E2 than during E1 possibly due to the more intensive

314   atmospheric aging. Similarly, during the two episodes (Fig. 3b,c), the relatively high fraction

315   of the rich-K and BB particles are more affected by the primary emissions when their peak

316   value of SPAMS-specific size distribution concentrate at < 300 nm, and > 300 nm are more

317   related to the aging process (Li et al., 2022b; Bi et al., 2011). Relatively greater fluctuation

318   for the large-size fractions (> 1.1 μm) could be explained by the low particle concentration (a

319   number less than 20). It should be pointed out that further application of this method would

320   require a co-located particle-sizing instrument to scale the size-resolved particle detection

321   efficiency. Both particle composition and size-dependent are the predominant impacting

322   factors on the particle detection efficiency of the SPAMS (Wenzel et al., 2003; Yang et al.,

323   2017; Healy et al., 2013).

324   To investigate the mixing state of the secondary species in the six main particle types,

325   the number fractions of six secondary markers ($^{97}HSO_4^-$, $^{195}H(HSO_4)_2^-$, $^{62}NO_3^-$, $^{18}NH_4^+$,

326    $^{58}C_2H_5NHCH_2^+$ and $^{89}HC_2O_4^-$) are calculated (Fig. 4). The presences of amine (*m/z*

327    $^{58}C_2H_5NHCH_2^+$) and sulfuric acid (*m/z* $^{195}H(HSO_4)_2^-$) signals are possibly indicative of the

328   water uptake (Chen et al., 2019) and acidic property of the particles (Rehbein et al., 2011),

329   respectively. The mixing states are obtained by the ratio of the number concentration of the

330   selected ions to each particle type.

331   The most abundant of $^{97}HSO_4^-$ and $^{18}NH_4^+$ fraction are seen in Ammonium (99% and

332   94%, *respectively*) and EC-aged (92% and 31%, *respectively*) particles, whereas much low

333   fraction of $^{62}NO_3^-$ is found (2% and 7%, *respectively*). These suggest that ammonium sulfate

334   is not a predominant form instead of ammonium nitrate (Zhang et al., 2013). The high

contribution of $^{97}HSO_4^-$ in EC-containing particles also suggests a significant influence of anthropogenically emitted sulfate precursors (e.g., SO_2) on the aging of EC-containing particles at the high altitude (Peng et al., 2016; Zhang et al., 2017a). Meanwhile, relatively high number fractions of $^{195}H(HSO_4)_2^-$ and $^{58}C_2H_5NHCH_2^+$ are also observed in Ammonium (63% and 60%) and EC-aged (4% and 19%) particles. These abundant mixtures potentially represent the high hygroscopicity of Ammonium and EC-aged particles, and their ability to neutralize the acidic particles of Ammonium particle (Sorooshian et al., 2007). Then, a moderate fraction of $^{97}HSO_4^-$ and $^{18}NH_4^+$ are seen on the rich-K (65%, 7%) and OC (56%, 4%) particles. In contrast, more $^{62}NO_3^-$ fraction contribute to the rich-K (38%) and OC (68%) particles, mainly affected by vehicle emissions and biomass burning (Text S1). Following BB (18%) and Dust (6%) particles are found in a relatively low fraction of $^{97}HSO_4^-$, while the moderate $^{62}NO_3^-$ accounts for 45% of the BB particle but only 3% of the Dust particle. Combined with the results of the minor $^{18}NH_4^+$ fraction (<1%) in BB and Dust particles suggests a relatively low degree of aging. In addition, oxalate ($^{89}HC_2O_4^-$), a representative component of secondary organic formation is mainly mixed with BB (13%) and rich-K (12%) particles. This is because the substantial precursors of oxalic acid, including acetate ($^{59}C_2H_3O_2^-$), methylglyoxal ($^{71}C_3H_3O_2^-$), glyoxylate ($^{73}C_2HO_3^-$), are emitted from biomass burning, and then oxalate heterogeneously formed in BB related particles (Zhang et al., 2019b; Zauscher et al., 2013). A relatively low fraction (<5%) of oxalate-containing particles in OC, Ammonium, EC-aged and Dust particles is potentially limited by the contributions of precursor oxalic acid.

Compared to the mixing state of individual particle in urban or suburban areas that are located close to emission sources (Chen et al., 2016; Dall′Osto and Harrison, 2012; Zhang et al., 2017a; Li et al., 2022b), the high fractions of sulfate and ammonium at the high altitude area demonstrate a high degree of aging of the individual particles, whereas the low fraction of nitrate with high volatility indicates its loss during transportation processing.

The number fractions of six markers in the four trajectories were used to further investigate the impacts of regional transport. As shown in Fig. 5(a,c), the dominant mixing ion types in each particles (except for Dust) are similar among the four clusters. For Cluster 1, the number fractions of $^{97}HSO_4^-$ and $^{89}HC_2O_4^-$ have larger values in five particle types

365 (except for Dust type) than those in other trajectories. Similar to Cluster 1, Cluster 3 and 4 are

366 impacted by regional transport from northeastern Myanmar, the fractions of the six markers

367 also similar in OC, Ammonium, and EC-aged types. However, $^{97}HSO_4^-$ in Cluster 3 and 4 is

368 reduced in rich-K, BB and Dust types, while $^{62}NO_3^-$ is increased in rich-K and decreased in

369 Dust types, compared with Cluster 1. As discussed in Section 3.1, these results demonstrate

370 that the aging degree of Cluster 3 and 4 might be lower than that of Cluster 1. For Cluster 2,

371 the fraction of $^{97}HSO_4^-$ is obviously decreased in rich-K, BB and EC-aged types but slightly

372 increased in Dust type (Fig. 5f). Such pattern inverse the observations in rich-K, OC and Dust

373 types for $^{62}NO_3^-$ ions. These variations in Cluster 2 are more likely due to the influences of

374 biomass-burning activities from surrounding the sampling site, rather than regional transport.

375 Furthermore, Cluster 2 is associated with regional transport from northeastern India along the

376 afternoon to nighttime (from 15:00 LT on 11 May to 07:00 LT on 12 May), which is

377 favorable to the nitrate formation N_2O_5 by heterogeneous hydrolysis (Wang et al., 2017; Ding

378 et al., 2021). However, these cases are infrequent, as only 2% of trajectories are associated

379 with Cluster 2.

380 During E1, more than 50% of $^{97}HSO_4^-$ fractions are mixed in the rich-K (81%), OC

381 (62%), Ammonium (100%), EC-aged (98%) particles (Fig. S12), low in BB (37%) and Dust

382 (4%) particles. Dissimilar with E1, the number fraction of $^{97}HSO_4^-$ in Dust increases to 34%

383 during E2, potentially associated with the enhancement by secondary formation during

384 regional transport. However, the mixing state of $^{195}H(HSO_4)_2^-$), $^{62}NO_3^-$, NH_4^+ and oxalate

385 fractions are similar between the two episode events. The $^{58}C_2H_5NHCH_2^+$ fractions are

386 significantly higher in E2 than E1 for Ammonium (67% versus 31%) and EC-aged particles

387 (48% versus 17%), due to the relatively higher hygroscopic behavior (i.e., RHs) (Sorooshian

388 et al., 2007).

389 **3.3 Formation process of the high number concentration particle episodes**

390 Photochemical oxidation and aqueous-phase reaction are the key formation pathways of

391 secondary species (Link et al., 2017; Xue et al., 2014; Jiang et al., 2019). The oxidant O_x (O_3

392 + NO_2) concentration and RH usually serve as indicators of the degree of photochemical

393 oxidation (Wood et al., 2010) and aqueous-phase reaction (Ervens et al., 2011), *receptively,*

394 though the current O_x and RH conditions obtained using the in-situ measurement are not

395   indicative of the past conditions experienced by the particle. Thus, the relative number

396   fractions of $^{43}C_2H_3O^+$, $^{89}HC_2O_4^-$, $^{62}NO_3^-$, $^{97}HSO_4^-$ and $^{18}NH_4^+$-containing particles to the total

397   detected particles were selected to provide a rough speculative of the secondary formation

398   mechanism in TP ambient conditions (Liang et al., 2022). The correlations of the number

399   fraction of each secondary species with the O_x concentrations (O_x) during daytime (from

400   06:00 to 20:00 LT) and RH during nighttime (from 20:00 to 06:00 LT next day) are used to

401   reveal the formation pathways during the two episodes (Li et al., 2022).

402   As illustrated in Fig. 6, for E1, $^{43}C_2H_3O^+$, $^{89}HC_2O_4^-$, $^{97}HSO_4^-$, and $^{18}NH_4^+$ show

403   significant negative linear correlations with O_x ($p < 0.01$), and the correlation strengths range

404   from moderate to strong (r = –0.51 to –0.81). However, the $^{62}NO_3^-$ fraction shows an upward

405   trend with an insignificant correlation (r = 0.33, $p > 0.05$) with the increase in O_x

406   concentration. For E2, $^{43}C_2H_3O^+$ shows weak correlation with O_x (r = 0.37, $p > 0.05$), but

407   strong correlations with $^{89}HC_2O_4^-$, $^{97}HSO_4^-$, and $^{18}NH_4^+$ (r = 0.81~0.92, $p < 0.01$). It should

408   be noted that $^{62}NO_3^-$ has a strong negative correlation (r =–0.85, $p < 0.01$) with O_x. In general,

409   the opposite linear relationship between secondary aerosol and O_x during E1 and E2 might be

410   influenced by reasons of i) the relatively low secondary formations because of the small

411   amount of precursors emitting from anthropogenic activities around the sampling site (Li et

412   al., 2016); ii) higher dilution rate of the particles formed in the atmosphere with the rapid rise

413   of PBL height during E1 than E2 (Fig. S13a); iii) the degrees of contributions of regional

414   transport due to the low WS (0.5 ± 0.6 m s^{-1}) during E1 and the high WS (3.1 ± 1.0 m s^{-1})

415   during E2, respectively (Fig. S9). Therefore, for E1, the increases of NO_3^- fraction could be

416   influenced by the local nitrate formation, while the declines of other secondary components

417   should be ascribed to the reduced contribution of regional transport. For E2, the decreased of

418   NO_3^- fraction could be caused by the relatively higher volatilization loss of nitrate than other

419   components through the regional transport. Additionally, previous study proves that the

420   formations of organic nitrate species (such as $^{27}CHN^+$, $^{30}NO^+$, $^{43}CHO_1N^+$ and CHO_xN^+)

421   through the NO+RO$_2$ pathway dominate 80% of the total nitrate production in tropical

422   forested regions during summertime (Alexander et al., 2009). Aruffo et al (2022) also found

423   that low NO_x (i.e. < 6 ppbv), compared to 2.3 ± 0.8 ppbv in this study, could even promote

424   the particle-phase partitioning of the lower volatility of organonitrates. These results suggest

that the secondary organic species have different formation capacities through photo-oxidation reactions, among which the rate of HSO_4^- formation (slop=0.017) is the highest. Increased with O_x concentration during E2, the concentration levels of secondary organic species of $C_2H_3O^+$ (18%-28%) imperceptibly rise, while the oxalate fraction significantly increase by 7%-20%.

Considering that the oxalate is abundant mixed in rich-K (14%), BB (15%), EC-aged (5%), and Dust (6%) particles in Cluster 1 (Fig. 5), and the increased contributions of rich-K (39.3%), BB (14.2%) and EC-aged (17.2%) types during E2 (Table 1), the apparent formation of oxalate might be due to the enhancement of regional transport. Particularity, this presents the nearby biomass burning and combustion activities produce more precursor species of oxalate (Sullivan et al., 2007; Kundu et al., 2010; Zhang et al., 2017b).

Fig. 7 illustrates that the number fractions of $^{43}C_2H_3O^+$, $^{89}HC_2O_4^-$, $^{97}HSO_4^-$, and $^{18}NH_4^+$ have moderate to strong positive correlations with RH (r = 0.70~0.81, p < 0.01 or 0.05) in the nighttime during the two episodes, except that $^{43}C_2H_3O^+$ during E2 (p = 0.48) and $^{89}HC_2O_4^-$ during E1 (p = 0.12). Furthermore, $^{62}NO_3^-$ fraction has no obvious changes with insignificant correlation with RH during E1 (p = 0.43) and presents a moderate negative correlation with RH (r = 0.69, p < 0.01) during E2. As shown in Fig. 7e, the highest aqueous formation rate of HSO_4^- is mainly due to the properties of low volatile and high hygroscopic of sulfate (Wang et al., 2016; Zhang et al., 2019c; Sun et al., 2013). Compared with that during E2 (slop=0.014), the decreased formation rate of HSO_4^- during the E1 (slop=0.009) may be because the decreases of aerosol acidity in higher RH > 80% (Huang et al., 2019; Meng et al., 2014; Tian et al., 2021). And the increased contributions of regional transport due to the high WS (2.4 ± 0.8 m s^{-1}) during E2 are compared with the low WS (0.08 ± 0.08 m s^{-1}) during E1 (Fig. S9). The fair production rate of NH_4^+ during the E1 (slop= 0.005) and E2 (slop=0.006) demonstrate that an aqueous-phase reaction could effectively promote ammonium formation. Meanwhile, a slightly larger slop of NH_4^+ during E2 could be also affected by the increased contributions of regional transport. Compared with those during E1, the inverse generation rates of two secondary organic species (i.e., $C_2H_3O^+$ and $HC_2O_4^-$) during E2 are possibly caused by the different formation pathways with a variety of RH levels or distinct regional transports. For example, $C_2H_3O^+$ shows a strong correlation with RH (r = 0.70, p < 0.05)

during E1 (slop=0.003) but has insignificant correlation during E2. This could be explained by high RHs that could effectively promote secondary organic formation during E1. In addition, the $HC_2O_4^-$ fraction increases slightly (9.7-13.1%) during E1 is potentially ascribed to more abundant Dust-type particles (20.3%) which compose of high calcium (Ca) (Fig. S14) that favor the formation of metal oxalate complexes (i.e., Ca oxalate). At high RHs (93.4 ± 7.6%), if oxalate ions are dissolved in the aqueous phase with the presence of Ca ions, the Ca oxalate complexes can precipitate because of their low hygroscopic and insoluble natures (Furukawa and Takahashi, 2011). This could offset the oxalate formation in the aqueous-phase reaction. However, significant linear increases (slop=0.003) with RH (r = 0.81, p < 0.01) during E2 demonstrate that the aqueous-phase reaction effectively promotes the oxalate formation (Cheng et al., 2017; Meng et al., 2020). No obvious change and insignificant correlation between $^{62}NO_3^-$ and RH are found during E1, potentially attributed to the decreases of NO_2 concentration (3.7 ± 0.4 ppbv) in the local atmosphere. Meanwhile, high RHs could promote organonitrates formation (Fang et al., 2021; Fry et al., 2014). The linearity between $^{62}NO_3^-$ and RH (r = 0.69, p < 0.01) significantly decreases during E2, mostly due to the losses of the volatile compound through the regional transport (Fig. S15).

4   Conclusions

This study presents the chemical composition, size distribution, mixing state and secondary formation of individual particles in the southeastern margin of TP, China during the pre-monsoon season using a high-resolution SPAMS. The finding shows that the rich-K (30.9%) and BB types (18.7%) are the two dominant aerosol particles in the remote area; followed by the OC (12.8%), Ammonium (11.9%), EC-aged (10.9%), and Dust (10.7%) types; the NaK-SN, Metal and Others particle types contributed 0.3–2.8% to the total ambient particles. By interpreting the mass spectra and diurnal trends, the major particle types are mainly from traffic emission, biomass burning, secondary formation and fly ash, while the dynamics of the PBL height could also affect their contributions. The observed change in the number fraction of the particle types was mainly influenced by air mass (97.61% of the total trajectories) from northeastern Myanmar, and significantly contributed to rich-K and BB types. The particle types show distinct size distributions. The two critical particle types of rich-K and BB appear in a unimodal pattern, the fractions of OC and EC-aged gradually

485   decrease with the increase of the particle sizes, but Ammonium and Dust types show the

486   opposite. Sulfate is the major secondary species and is highly mixed with rich-K, Ammonium

487   and EC-aged types. Nitrate has a relatively low mixing ratio due to its higher volatility than

488   sulfate during regional transportation, except for BB and OC types. During the entire study

489   campaign, two episodes with the high number concentration of particles occur but with

490   significant differences in each particle fraction due to the different meteorological conditions

491   (RH, WS, etc.). Meanwhile, the different meteorological conditions also lead to an inverse

492   linear correlation between the indicators of secondary formation, including $C_2H_3O^+$, $HC_2O_4^-$,

493   NH_4^+, NO_3^- and HSO_4^-. and O_x (O_3+NO_2) during episode 1 and 2 periods; however, they

494   present a positive linear correlation with relative humidity (RH), except for NO_3^- shown the

495   negative linear correlation with RH due to the low precursors concentration and potential

496   organonitrates formation. These results demonstrated that the capacity of atmospheric aging

497   of photo-oxidation and aqueous reaction have complex influencing factors. Although the

498   detailed formation pathways and their percentage contributions to secondary species are not

499   quantitatively estimated in this study, our results have important implications for the various

500   possibilities affecting the characteristic of chemical components, size distribution, mixing

501   states, and formation mechanism of aerosols in the southeast TP. More depth investigations

502   concerning the evolution mechanisms of secondary aerosols are encouraged since TP is a

503   significant regulator to global climate change.

504 *Data availability*. The data presented in this study are available at the Zenodo data archive

505 https://doi.org/10.5281/zenodo.7336857.

506

507 *Competing interests*. The authors declare that they have no conflict of interest.

508

509 *Author contributions*. QW and JC designed the campaign. WR conducted field measurements.

510 LL, QW, JT, and YZ made data analysis and interpretation. LL and QW wrote the paper. All

511 the authors reviewed and commented on the paper.

512

513 *Acknowledgments*. The authors are grateful to the staff from Lijiang Astronomical Station for

514 their assistance with field sampling. The authors are also grateful to Weikang Ran, Yonggang

515 Zhang, and other staff for the field observation.

516

517 *Financial support*. This work was supported by the Second Tibetan Plateau Scientific

518 Expedition and Research Program (STEP) (2019QZKK0602), the National Natural Science

519 Foundation of China (41877391), and the Youth Innovation Promotion Association of the

520 Chinese Academy of Sciences (2019402).

521

Reference

523 Alexander, B., Hastings, M. G., Allman, D. J., Dachs, J., Thornton, J. A., and Kunasek, S. A.: Quantifying
524   atmospheric nitrate formation pathways based on a global model of the oxygen isotopic composition
525   (Δ^{17}O) of atmospheric nitrate, Atmos. Chem. Phys., 9, 5043–5056,
526   https://doi.org/10.5194/acp-9-5043-2009, 2009.

527 Allen, J. O., Fergenson, D. P., Gard, E. E., Hughes, L. S., Morrical, B. D., Kleeman, M. J., Gross, D. S.,
528   Gälli, M. E., Prather, K. A., and Cass, G. R.: Particle Detection Efficiencies of Aerosol Time of Flight
529   Mass Spectrometers under Ambient Sampling Conditions, Environ. Sci. Technol., 34, 211-217,
530   https://doi.org/10.1021/es9904179, 2000.

531 Aruffo, E., Wang, J., Ye, J., Ohno, P., Qin, Y., Stewart, M., McKinney, K., Di Carlo, P., and Martin, S. T.:
532   Partitioning of Organonitrates in the Production of Secondary Organic Aerosols from α-Pinene
533   Photo-Oxidation, Environ. Sci. Technol., 56, 5421–5429, https://doi.org/10.1021/acs.est.1c08380,
534   2022.

535 Bi, X. H., Zhang, G. H., Li, L., Wang, X. M., Li, M., Sheng, G. Y., Fu, J. M., and Zhou, Z.: Mixing state of
536   biomass burning particles by single particle aerosol mass spectrometer in the urban area of PRD,
537   China, Atmos. Environ., 45, 3447–3453, https://doi.org/10.1016/j.atmosenv.2011.03.034, 2011.

538 Bi, X. H., Lin, Q. H., Peng, L., Zhang, G. H., Wang, X. M., Brechtel, F. J., Chen, D. H., Li, M., Peng, P. A.,

Sheng, G. Y., and Zhou, Z.: In situ detection of the chemistry of individual fog droplet residues in the Pearl River Delta region, China, J. Geophys. Res. Atmos., 121, 9105–9116, https://doi.org/10.1002/2016jd024886, 2016.

Budisulistiorini, S. H., Riva, M., Williams, M., Chen, J., Itoh, M., Surratt, J. D., and Kuwata, M.: Light-absorbing brown carbon aerosol constituents from combustion of Indonesian peat and biomass, Environ. Sci. Technol., 51, 4415-4423, https://doi.org/10.1021/acs.est.7b00397, 2017.

Canagaratna, M. R., Jayne, J. T., Jimenez, J. L., Allan, J. D., Alfarra, M. R., Zhang, Q., Onasch, T. B., Drewnick, F., Coe, H., Middlebrook, A., Delia, A., Williams, L. R., Trimborn, A. M., Northway, M. J., DeCarlo, P. F., Kolb, C. E., Davidovits, P., and Worsnop, D. R.: Chemical and microphysical characterization of ambient aerosols with the aerodyne aerosol mass spectrometer, Mass Spectrom. Rev., 26, 185–222, https://dx.doi.org/10.1002/mas.20115, 2007.

Chan, C. Y., Wong, K. H., Li, Y. S., Chan, Y., and Zhang, X.D.: The effects of Southeast Asia fire activities on tropospheric ozone, trace gases and aerosols at a remote site over the Tibetan Plateau of Southwest China, Tellus B, 58B, 310–318, https://doi.org/10.1111/j.1600-0889.2006.00187.x, 2017.

Chen, Y., Cao, J. J., Huang, R. J., Yang, F. M., Wang, Q. Y., and Wang, Y. C.: Characterization, mixing state, and evolution of urban single particles in Xi'an (China) during wintertime haze days, Sci. Total Environ., 573, 937–945, https://doi.org/10.1016/j.scitotenv.2016.08.151, 2016.

Chen, Y., Wenger, J. C., Yang, F. M., Cao, J. J., Huang, R. J., Shi, G. M., Zhang, S. M., Tian, M., and Wang, H. B.: Source characterization of urban particles from meat smoking activities in Chongqing, China using single particle aerosol mass spectrometry, Environ. Pollut., 228, 92–101, https://doi.org/10.1016/j.envpol.2017.05.022, 2017.

Chen, Y., Tian, M., Huang, R. J., Shi, G. M., Wang, H. B., Peng, C., Cao, J. J., Wang, Q. Y., Zhang, S. M., Guo, D. M., Zhang, L. M., and Yang, F. M.: Characterization of urban amine-containing particles in southwestern China: seasonal variation, source, and processing, Atmos. Chem. Phys., 19, 3245–3255, https://doi.org/10.5194/acp-19-3245-2019, 2019.

Chen, J. Q., and Bordoni, S.: Orographic effects of the Tibetan Plateau on the East Asian Summer Monsoon: An energetic perspective, J. Climate., 27, 3052–3072, https://doi.org/10.1175/JCLI-D-13-00479.1, 2014.

Cheng, C. L., Li, M., Chan, C. K., Tong, H. J., Chen, C. H., Chen, D. H., Wu, D., Li, L., Wu, C., Cheng, P., Gao, W., Huang, Z. X., Li, X., Zhang, Z. J., Fu, Z., Bi, Y. R., Zhou, Z.: Mixing state of acid containing particles in the rural area of Pearl River Delta, China: implicatio the formation mechanism of oxalic acid, Atmos. Chem. Phys., 17, 9519–9533, https://doi.org/10.5194/acp-17-9519-2017, 2017.

Crippa, M., DeCarlo, P. F., Slowik, J. G., Mohr, C., Heringa, M. F., Chirico, R., Poulain, L., Freutel, F., Sciare, J., Cozic, J., Di Marco, C. F., Elsasser, M., Nicolas, J. B., Marchand, N., Abidi, E., Wiedensohler, A., Drewnick, F., Schneider, J., Borrmann, S., Nemitz, E., Zimmermann, R., Jaffrezo, J. L., Prévôt, A. S. H., and Baltensperger, U.: Wintertime aerosol chemical composition and source apportionment of the organic fraction in the metropolitan area of Paris, Atmos. Chem. Phys., 13, 961–981, https://doi.org/10.5194/acp-13-961-2013, 2013.

Dall'Osto, M., Beddows, D.C.S., Gietl, J. K., Olatunbosun, O. A., Yang, X. G., and Harrison, R. M.: Characteristics of tyre dust in polluted air: studies by single particle mass spectrometry (ATOFMS), Atmos. Environ., 94, 224–230, https://doi.org/10.1016/j.atmosenv.2014.05.026, 2014.

Dall'Osto, M., and Harrison, R. M.: Urban organic aerosols measured by single particle mass spectrometry in the megacity of London, Atmos. Chem. Phys., 12, 4127–4142, http://dx.doi.org/10.5194/acp-12-4127–2012, 2012.

Ding, J., Dai, Q. L., Zhang, Y. F., Xu, J., Huangfu, Y. Q., Feng, Y. C.: Air humidity affects secondary aerosol formation in different pathways, Sci. Total Environ., 759, 143540–143549, https://doi.org/10.1016/j.scitotenv.2020.143540, 2021.

Draxler, R. and Hess, G.: An overview of the HYSPLIT_4 modelling system for trajectories, Aust. Meteorol. Mag., 47, 295–308, 1998.

Du, W., Sun, Y. L., Xu, Y. S., Jiang, Q., Wang, Q. Q., Wang, W., Wang, F., Bai, Z. P., Zhao, X. D., and Yang, Y. C.: Chemical characterization of submicron aerosol and particle growth events at a national background site (3295 m a.s.l.) on the Tibetan Plateau, Atmos. Chem. Phys., 15, 10811–10824, https://doi.org/10.5194/acp-15-10811-2015, 2015.

Engling, G., Zhang, Y. N., Chan, C. Y., Sang, X. F., Lin, M., Ho, K. F., Li, Y. S., Lin, C. Y., and Lee, J. J.: Characterization and sources of aerosol particles over the southeastern Tibetan Plateau during the Southeast Asia biomass-burning season, Tellus B, 63, 117–128, https://doi.org/10.1111/j.1600-0889.2010.00512.x, 2011.

Ervens, B., Turpin, B. J., and Weber, R. J.: Secondary organic aerosol formation in cloud droplets and aqueous particles (aqSOA): a review of laboratory, field and model studies, Atmos. Chem. Phys., 11, 11069–11102, https://doi.org/10.5194/acp-11-11069-2011, 2011.

Fang, X. Z., Liu, Y. Y., Li, K. J., Wang, T., Deng, Y., Feng, Y. Q., Yang, Y., Cheng, H. Y., Chen, J. M., and Zhang, L. W.: Atmospheric Nitrate Formation through Oxidation by Carbonate Radical, ACS Earth Space Chem., 5, 1801–1811, https://doi.org/10.1021/acsearthspacechem.1c00169, 2021.

Fry, J. L., Draper, D. C., Barsanti, K. C., Smith, J. N., Ortega, J., Winkler, P. M., Lawler, M. J., Brown, S. S., Edwards, P. M., Cohen, R. C., and Lee, L.: Secondary Organic Aerosol Formation and Organic Nitrate Yield from NO_3 Oxidation of Biogenic Hydrocarbons, Environ. Sci. Technol., 48, 11944–11953, https://doi.org/10.1021/es502204x, 2014.

Furukawa, T., and Takahashi, Y.: Oxalate metal complexes in aerosol particles: implications for the hygroscopicity of oxalate-containing particles, Atmos. Chem. Phys., 11, 4289–4301, https://doi.org10.5194/acp-11-4289-2011, 2011.

Gettelman, A., Morrison, H., Terai, C. R., and Wood, R.: Microphysical process rates and global aerosolecloud interactions, Atmos. Chem. Phys., 13, 9855–9867, https://doi.org/10.5194/acp-14-9099-2014, 2013.

Han, H., Wu, Y., Liu, J., Zhao, T. L., Zhuang, B. L., Wang, H. L., Li, Y. C., Chen, H. M., Zhu, Y., Liu, H. N., Wang, Q. G., Li, S., Wang, T. J., Xie, M., and Li, M. M.: Impacts of atmospheric transport and biomass burning on the inter-annual variation in black carbon aerosols over the Tibetan Plateau, Atmos. Chem. Phys., 20, 13591–13610, https://doi.org/10.5194/acp-20-13591-2020, 2020.

Healy, R. M., Sciare, J., Poulain, L., Crippa, M., Wiedensohler, A., Prévôt, A.S.H., Baltensperger, U., Sarda-Estève, R., McGuire, M. L., Jeong, C. H., McGillicuddy, E., O'Connor, I. P., Sodeau, J. R., Evans, G. J., and Wenger, J. C.: Quantitative determination of carbonaceous particle mixing state in Paris using single-particle mass spectrometer and aerosol mass spectrometer measurements, Atmos. Chem. Phys., 13, 9479–9496, http://dx.doi.org/10.5194/acp-13-9479-2013, 2013.

Hua, S., Liu, Y. Z., Luo, R., Shao, T. B., Zhu, Q. Z.: Inconsistent aerosol indirect effects on water clouds and ice clouds over the Tibetan Plateau, Int. J. Climatol., 40, 3832–3848, https://doi.org/10.1002/joc.6430, 2019.

Huang, X. J., Zhang, J. K., Luo, B., Luo, J. Q., Zhang, W., and Rao, Z. H.: Characterization of oxalic acid-containing particles in summer and winter seasons in Chengdu China, Atmos. Environ., 198, 133–141, https://doi.org/10.1016/j.atmosenv.2018.10.050, 2019.

Immerzeel, W. W., van Beek, L. P. H., and Bierkens, M. F. P.: Climate change will affect the Asian water towers, Science, 328, 1382–1385, https://doi.org/10.1126/science.1183188, 2010.

Jacobson, M. Z.: Analysis of aerosol interactions with numerical techniques for solving coagulation, nucleation, condensation, dissolution, and reversible chemistry among multiple size distributions, J. Geophys. Res., 107(D19), 4366, https://doi.org/10.1029/2001JD002044, 2002.

Jiang, H. H., Frie, A. L., Lavi, A., Chen, J. Y., Zhang, H., Bahreini, R., and Lin, Y. H.: Brown carbon formation from nighttime chemistry of unsaturated heterocyclic volatile organic compounds, Environ. Sci. Technol. Lett., 6, 184190, https://doi.org/10.1021/acs.estlett.9b00017, 2019.

Kumar, M., Raju, M. P., Singh, R. K., Singh, A. K., Singh, R. S., and Banerjee, T.: Wintertime characteristics of aerosols over middle Indo-Gangetic Plain: vertical profile, transport and radiative forcing, Atmos. Res., 183, 268–282, https://doi.org/10.1016/j.atmosres.2016.09.012, 2017.

Kundu, S., Kawamura, K., Andreae, T. W., Hoffer, A., and Andreae, M. O.: Molecular distributions of dicarboxylic acids, ketocarboxylic acids and alpha-dicarbonyls in biomass burning aerosols: implications for photochemical production and degradation in smoke layers, Atmos. Chem. Phys., 10 (5), 2209−2225, https://doi.org/10.5194/acp-10-2209-2010, 2010.

Lian, X. F., Zhang, G. H., Yang, Y. X., Lin, Q. H., Fu, Y. Z., Jiang, F., Peng, L., Hu, X. D., Chen, D. H., Wang, X. M., Peng, P. A., Sheng, G. Y., and Bi, X. H.: Evidence for the Formation of Imidazole from Carbonyls and Reduced Nitrogen Species at the Individual Particle Level in the Ambient Atmosphere, Environ. Sci. Technol. Lett., 8, 9–15, https://dx.doi.org/10.1021/acs.estlett.0c00722, 2021.

Liang, Z. C., Zhou, L. Y., Cuevas, R. A., Li, X. Y., Cheng, C. L., Li, M., Tang, R. Z., Zhang, R. F., Lee Patrick K. H., Lai, Alvin C. K., and Chan, C.K.: Sulfate Formation in Incense Burning Particles: A Single-Particle Mass Spectrometric Study, Environ. Sci. Technol. Lett., 9, 718–725, https://doi.org/10.1021/acs.estlett.2c00492, 2022.

Li, C. L., Bosch, C., Kang, S. C., Andersson, A., Chen, P. F., Zhang, Q. G., Cong, Z. Y., Chen, B., Qin, D. H., and Gustafsson., Ö.: Sources of black carbon to the Himalayan–Tibetan Plateau glaciers, Nat. Commun., 7, 12574, https://doi.org/10.1038/ncomms12574, 2016b.

Li, C. L., Bosch, C., Kang, S. C., Andersson, A., Chen, P. F., Zhang, Q. G., Cong, Z. Y., Tripathee, L., and Örjanb, G.: [14]C characteristics of organic carbon in the atmosphere and at glacier region of the Tibetan Plateau, Sci. Total Environ., 832, 155020, https://doi.org/10.1016/j.scitotenv.2022.155020, 2022a.

Li, L., Huang, Z. X., Dong, J. G., Li, M., Gao, W., Nian, H. Q., Fu, Z., Zhang, G. H., Bi, X. H., Cheng, P., and Zhou, Z.: Real time bipolar time-of-flight mass spectrometer for analyzing single aerosol particles, Int. J. Mass Spectrom., 303, 118–124, https://doi.org/10.1016/j.ijms.2011.01.017, 2011.

Li L., Wang, Q. Y., Zhang, Y., Liu, S. X., Zhang, T., Wang, S., Tian, J., Chen, Y., Hang Ho, S. S., Han, Y., and Cao, J.J.: Impact of reduced anthropogenic emissions on chemical characteristics of urban aerosol by individual particle analysis, Chemosphere, 303, 135013, https://doi.org/10.1016/j.chemosphere.2022.135013, 2022b.

Li, J. J., Wang, G. H., Wang, X. M., Cao, J. J., Sun, T., Cheng, C. L., Meng, J. J., Hu, T. F., and Liu, S. X.: Abundance, composition and source of atmospheric $PM_{2.5}$ at a remote site in the Tibetan Plateau, China, Tellus B, 65, http://dx.doi.org/10.3402/tellusb.v65i0.20281, 2013.

Li, Y. J., Sun, Y. L., Zhang, Q., Li, X., Li, M., Zhou, Z., and Chan, C. K.: Real-time chemical characterization of atmospheric particulate matter in China: A review, Atmos. Environ., 158, 270–304, http://dx.doi.org/10.1016/j.atmosenv.2017.02.027, 2017.

Lin, Q. H., Bi, X. H., Zhang, G. H., Yang, Y. X., Peng, L., Lian, X. F., Fu, Y. Z., Li, M., Chen, D. H., Miller, M., Ou, J., Tang, M. J., Wang, X. M., Peng, P. A., Sheng, G. Y., and Zhou, Z.: In-cloud formation of

secondary species in iron-containing particles, Atmos. Chem. Phys., 19, 1195–1206, https://doi.org/10.5194/acp-19-1195-2019, 2019.

Link, M. F., Kim, J., Park, G., Lee, T., Park, T., Babar, Z. B., Sung, K., Kim, P., Kang, S., Kim, J. S., Choi, Y., Son, J., Lim, H. J., and Farmer, D.K.: Elevated production of NH_4NO_3 from the photochemical processing of vehicle exhaust: Implications for air quality in the Seoul Metropolitan Region, Atmos. Environ., 156, 95–101, https://doi.org/10.1016/j.atmosenv.2017.02.031, 2017.

Liu, Y. Z., Zhu, Q. Z., Huang, J. P., Hua, S., and Jia, R.: Impact of dust-polluted convective clouds over the Tibetan Plateau on downstream precipitation, Atmos. Environ., 209, 67–77, https://doi.org/10.1016/j.atmosenv.2019.04.001, 2019.

Liu, Q., Liu, D. T., Gao, Q., Tian, P., Wang, F., Zhao, D. L., Bi, K., Wu, Y. Z., Ding, S., Hu, K., Zhang, J. L., Ding, D. P., and Zhao, C. S.: Vertical characteristics of aerosol hygroscopicity and impacts on optical properties over the North China Plain during winter, Atmos. Chem. Phys., 20, 3931–3944, https://doi.org/10.5194/acp-20-3931-2020, 2020a.

Liu, D. T., Hu, K., Zhao, D. L., Ding, S., Wu, Y. F., Zhou, C., Yu, C. J., Tian, P., Liu, Q., Bi, K., Wu, Y. Z., Hu, B., Ji, D. S., Kong, S. F., Ouyang, B., He, H., Huang, M. Y., and Ding, D.P.: Efficient Vertical Transport of Black Carbon in the Planetary Boundary Layer, Geo. Res. Lett., 47, 1–10, https://doi.org/10.1029/2020GL088858, 2020b

Liu, H. K., Wang, Q. Y., Xing, L., Zhang, Y., Zhang, T., Ran, W. K., and Cao, J. J.: Measurement report: quantifying source contribution of fossil fuels and biomass-burning black carbon aerosol in the southeastern margin of the Tibetan Plateau, Atmos. Chem. Phys., 21, 973–987, https://doi.org/10.5194/acp-21-973-2021, 2021.

Liu, X. D., Dong, B. W., Yin, Z. Y., Smith, R. S., Guo, Q. C.: Continental drift and plateau uplift control origination and evolution of Asian and Australian monsoons, Sci. Rep., 7, 40344, https://doi.org/10.1038/srep40344, 2017.

Luo, M., Liu, Y. Z., Zhu, Q. Z., Tang, Y. H., and Alam, K.: Role and mechanisms of black carbon affecting water vapor transport to Tibet, Remote Sens., 12, 231, https://doi.org/10.3390/rs12020231, 2020.

Ma, L., Li, M., Huang, Z. X., Li, L., Gao, W., Nian, H. Q., Zou, L. L., Fu, Z., Gao, J., Chai, F. H., and Zhou, Z.: Real time analysis of lead-containing atmospheric particles in Beijing during springtime by single particle aerosol mass spectrometry, Chemosphere, 154, 454–462, https://doi.org/10.1016/j.chemosphere.2016.04.001, 2016.

Ma, X., Yu, F., and Luo, G.: Aerosol direct radiative forcing based on GEOS-Chem-APM and uncertainties, Atmos. Chem. Phys., 12, 5563–5581, https://doi.org/10.5194/acp-12-5563-2012, 2012.

Matsui, H.: Black carbon simulations using a size- and mixingstate-resolved three-dimensional model: 2. Aging timescale and its impact over East Asia, J. Geophys. Res. Atmos., 121, 1808–1821, https://doi.org/10.1002/2015jd023999, 2016.

Meng, J. J, Wang, G. H, Li, J. J, Cheng, C. L, Ren, Y. Q, Huang, Y., Cheng, Y. T, Cao, J. J, and Zhang, T.: Seasonal characteristics of oxalic acid and related SOA in the free troposphere of Mt. Hua, central China: implications for sources and formation mechanisms, Sci. Total Environ., 493, 1088–1097, https://doi.org/10.1016/j.scitotenv.2014.04.086, 2014.

Meng, J. J., Liu, X. D., Hou, Z. F., Yi, Y. N., Yan, L., Li, Z., Cao, J.J., Li, J. J., Wang, G. H.: Molecular characteristics and stable carbon isotope compositions of dicarboxylic acids and related compounds in the urban atmosphere of the North China Plain: implications for aqueous phase formation of SOA during the haze periods, Sci. Total Environ., 705, 135256, https://doi.org/10.1016/j.scitotenv.2019.135256, 2020.

715 Ng, N. L., Canagaratna, M. R., Jimenez, J. L., Chhabra, P. S., Seinfeld, J. H., and Worsnop, D. R.: Changes
716   in organic aerosol composition with aging inferred from aerosol mass spectra, Atmos. Chem. Phys.,
717   11(13), 6465–6474, https://doi.org/10.5194/acp-11-6465-2011, 2011.

718 Peng, J. F., Hu, M., Guo, S., Du, Z. F., Zheng, J., Shang, D. J., Zamora, M. L., Zeng, L. M., Shao, M., Wu,
719   Y. S., Zheng, J., Wang, Y., Glen, C. R., Collins, D. R., Molina, M. J., and Zhang, R. Y.: Markedly
720   enhanced absorption and direct radiative forcing of black carbon under polluted urban environments,
721   P. Natl. Acad. Sci. USA, 113, 4266–4271, https://doi.org/10.1073/pnas.1602310113, 2016.

722 Pratt, K. A., Hatch, L. E., and Prather, K. A.: Seasonal volatility dependence of ambient particle phase
723   amines, Environ. Sci. Technol., 43, 5276–5281, https://doi.org/10.1021/es803189n, 2009.

724 Pratt, K. A., Murphy, S. M., Subramanian, R., DeMott, P. J., Kok, G. L., Campos, T., Rogers, D. C., Prenni,
725   A. J., Heymsfield, A. J., Seinfeld, J. H., and Prather, K. A.: Flight-based chemical characterization of
726   biomass burning aerosols within two prescribed burn smoke plumes, Atmos. Chem. Phys., 11,
727   12549–12565, https://doi.org/10.5194/acp-11-12549-2011, 2011.

728 Qian, Y., Flanner, M. G., Leung, L. R., and Wang, W.: Sensitivity studies on the impacts of Tibetan Plateau
729   snowpack pollution on the Asian hydrological cycle and monsoon climate, Atmos. Chem. Phys., 11,
730   1929-1948, https://doi.org/10.5194/acp-11-1929-2011, 2011.

731 Rehbein, P. J., Jeong, C. H., McGuire, M. L., Yao, X., Corbin, J. C., and Evans, G. J.: Cloud and fog
732   processing enhanced gas-toparticle partitioning of trimethylamine, Environ. Sci. Technol., 45,
733   4346–4352, https://doi.org/10.1021/es1042113, 2011.

734 Roth, A., Schneider, J., Klimach, T., Mertes, S., van Pinxteren, D., Herrmann, H., and Borrmann, S.:
735   Aerosol properties, source identification, and cloud processing in orographic clouds measured by
736   single particle mass spectrometry on a central European mountain site during HCCT-2010, Atmos.
737   Chem. Phys., 16, 505–524, https://doi.org/10.5194/acp-16-505-2016, 2016.

738 Shen, L. J., Wang, H. L., Yin, Y., Chen, J. H., and Chen, K.: Observation of atmospheric new particle
739   growth events at the summit of mountain Tai (1534 m) in Central East China, Atmos. Environ., 201,
740   148–157, https://doi.org/10.1016/j.atmosenv.2018.12.051, 2019.

741 Shen, L. J., Wang, H. L., Lü, S., Zhang, X. H., Yuan, J., Tao, S. K., Zhang, G. J., Wang, F., and Li, L.:
742   Influence of pollution control on air pollutants and the mixing state of aerosol particles during the 2nd
743   World Internet Conference in Jiaxing, China, J. Clean. Prod., 149, 436–447,
744   https://doi.org/10.1016/j.jclepro.2017.02.114, 2017.

745 Shen, R. Q., Ding, X., He, Q. F., Cong, Z. Y., Yu, Q. Q., and Wang, X. M.: Seasonal variation of secondary
746   organic aerosol tracers in Central Tibetan Plateau, Atmos. Chem. Phys., 15, 8781-8793,
747   https://doi.org/10.5194/acp-15-8781-2015, 2015.

748 Sirois, A. and Bottenheim, J. W.: Use of backward trajectories to interpret the 5-year record of PAN and O₃
749   ambient air concentrations at Kejimkujik National Park, Nova Scotia, J. Geophys. Res., 100,
750   2867–2881, https://doi.org/10.1029/94JD02951, 1995.

751 Song, X. H., and Hopke, P. K.: Classifcation of single particles analyzed by ATOFMS using an artifcial
752   neural network, ART-2A, Anal. Chem., 71, 860–865, https://doi.org/10.1021/ac9809682, 1999.

753 Sorooshian, A., Lu, M. L., Brechtel, F. J., Jonsson, H., Feingold, G., Flagan, R. C., and Seinfeld, J. H.: On
754   the source of organic acid aerosol layers above clouds, Environ. Sci. Technol., 41, 4647–4654,
755   https://doi.org/10.1021/es0630442, 2007.

756 Sullivan, R. C., Guazzotti, S. A., Sodeman, D. A., and Prather, K. A.: Direct observations of the
757   atmospheric processing of Asian mineral dust, Atmos. Chem. Phys., 7, 1213–1236,
758   https://doi.org/10.5194/acp-7-1213-2007, 2007.

Sun, Y. L, Wang, Z. F., Fu, P. Q., Jiang, Q. J., Yang, T., Li, J., and Ge, X. L.: The impact of relative humidity on aerosol composition and evolution processes during wintertime in Beijing, China, Atmos. Environ., 77, 927–934, https://doi.org/10.1016/j.atmosenv.2013.06.019, 2013.

Tian, J., Wang, Q. Y., Zhang, Y., Yan, M. Y., Liu, H. K., Zhang, N. N., Ran, W. K., and Cao, J. J.: Impacts of primary emissions and secondary aerosol formation on air pollution in an urban area of China during the COVID-19 lockdown, Environ. Int., 150, 106426–14, https://doi.org/10.1016/j.envint.2021.106426, 2021.

Wang, A. Q., Xie, X. N., Liu, X. D., and Yin, Z. Y.: Direct Radiative Effect (DRE) of Dust Aerosols on West African and East Asian Monsoon: The Role of Ocean-Atmosphere Interactions, J. Geophys. Res. Atmos., 127, 1–20, https://doi.org/10.1029/2021JD035917, 2022.

Wang, G. H., Zhang, R. Y., Gomez, M. E., Yang, L. X., Zamora, M. L., Hu, M., Lin, Y., Peng, J. F., Guo, S., Meng, J. J., Li, J. J., Cheng, C. L., Hu, T. F., Ren, Y. Q., Wang, Y. S., Gao, J., Cao, J. J., An, Z. S., Zhou, W. J., Li, G. H., Wang, J. Y., Tian, P. F., Marrero-Ortiz, W., Secrest, J., Du, Z. F., Zheng, J., Shang, D. J., Zeng, L. M., Shao, M., Wang, W. G., Huang, Y., Wang, Y., Zhu, Y. J., Li, Y. X., Hu, J. X., Pan, B. W., Cai, L., Cheng, Y. T., Ji, Y. M., Zhang, Y., Rosenfeld, D., Liss, P. S., Duce, R. A., Kolb, C. E., and Molina., M. J.: Persistent sulfate formation from London Fog to Chinese haze, P. Natl. Acad. Sci. USA, 113(48), 13630–13635, https://doi.org/10.1073/pnas.1616540113, 2016.

Wang, H. C., Lu, K. D., Chen, X. R., Zhu, Q. D., Chen, Q., Guo, S., Jiang, M. Q., Li, X., Shang, D. J., Tan, Z. F., Wu, Y. S., Wu, Z. J., Zou, Q., Zheng, Y., Zeng, L. M., Zhu, T., Hu, M., Zhang, Y. H.: High N2O5 concentrations observed in urban Beijing: implications of a large nitrate formation pathway, Environ. Sci. Technol. Lett., 4, 416–420, https://doi.org/10.1021/acs.estlett.7b00341, 2017.

Wang, H. L., An, J. L., Shen, L. J., Zhu, B., Xia, L., Duan, Q., and Zou, J. N.: Mixing state of ambient aerosols in Nanjing city by single particle mass spectrometry, Atmos. Environ., 132, 123–132, https://dx.doi.org/10.1016/j.atmosenv.2016.02.032, 2016.

Wang, Q. Y., Han, Y. M., Ye, J. H., Liu, S. X., Pongpiachan, S., Zhang, N. N., Han, Y. M., Tian, J., Wu, C., Long, X., Zhang, Q., Zhang, W. Y., Zhao, Z. Z., and Cao, J. J.: High contribution of secondary brown carbon to aerosol light absorption in the southeastern margin of Tibetan Plateau, Geophys. Res. Lett., 46, 4962–4970, https://doi.org/10.1029/2019GL082731, 2019a.

Wang, H. L., Shen, L. J., Yin, Y., Chen, K., Chen, J. H., and Wang, Y. S.: Characteristics and mixing state of aerosol at the summit of Mount Tai (1534 m) in Central East China: First measurements with SPAMS, Atmos. Environ., 213, 273–284, https://doi.org/10.1016/j.atmosenv.2019.06.021, 2019b.

Wang, Q. Y., Cao, J. J., Han, Y. M., Tian, J., Zhu, C. S., Zhang, Y., Zhang, N. N., Shen, Z. X., Ni, H. Y., Zhao, S. Y., and Wu, J. R.: Sources and physicochemical characteristics of black carbon aerosol from the southeastern Tibetan Plateau: internal mixing enhances light absorption, Atmos. Chem. Phys., 18, 4639–4656, https://doi.org/10.5194/acp-18-4639-2018, 2018.

Wenzel, R. J., Liu, D.-Y., Edgerton, E. S., and Prather, K. A.: Aerosol time-of-flight mass spectrometry during the Atlanta Supersite Experiment: 2. Scaling procedures, J. Geophys. Res., 108, 8427, http://dx.doi.org/10.1029/2001jd001563, 2003.

Wood, E. C., Canagaratna, M. R., Herndon, S. C., Onasch, T. B., Kolb, C. E., Worsnop, D. R., Kroll, J. H., Knighton, W. B., Seila, R., Zavala, M., Molina, L. T., DeCarlo, P. F., Jimenez, J. L., Weinheimer, A. J., Knapp, D. J., Jobson, B. T., Stutz, J., Kuster, W. C., and Williams, E. J.: Investigation of the correlation between odd oxygen and secondary organic aerosol in Mexico City and Houston, Atmos. Chem. Phys., 10, 8947–8968, https://doi.org/10.5194/acp-10-8947-2010, 2010.

Xu, L. L., Wu, X., Hong, Z. Y., Zhang, Y. R., Deng, J. J., Hong, Y. W., and Chen, J. S.: Composition,

mixing state, and size distribution of single submicron particles during pollution episodes in a coastal city in southeast China, Environ. Sci. Pollut. Res., 26, 1464–1473, https://doi.org/10.1007/s11356-018-3469-x, 2018.

Xu, W. Q., Han, T. T., Du, W., Wang, Q. Q., Chen, C., Zhao, J., Zhang, Y. J., Li, J., Fu, P. Q., Wang, Z. F., Worsnop, D. R., and Sun, Y. L.: Effects of aqueous-phase and photochemical processing on secondary organic aerosol formation and evolution in Beijing, China, Environ. Sci. Technol., 51, 762−770, https://doi.org/10.1021/acs.est.6b04498, 2017.

Xue, J., Griffth, S. M., Yu, X., Lau, A.K.H., and Yu, J. Z.: Effect of nitrate and sulfate relative abundance in $PM_{2.5}$ on liquid water content explored through half-hourly observations of inorganic soluble aerosols at a polluted receptor site, Atmos. Environ., 99, 24–31, https://doi.org/10.1016/j.atmosenv.2014.09.049, 2014.

Yang, J., Ma, S. X., Gao, B., Li, X. Y., Zhang, Y. J., Cai, J., Li, M., Yao, L. A., Huang, B., and Zheng, M.: Single particle mass spectral signatures from vehicle exhaust particles and the source apportionment of on-line $PM_{2.5}$ by single particle aerosol mass spectrometry, Sci. Total Environ., 593, 310–318, https://doi.org/10.1016/j.scitotenv.2017.03.099, 2017.

Zauscher, M. D., Wang, Y., Moore, M. J. K., Gaston, C. J., and Prather, K. A.: Air Quality Impact and Physicochemical Aging of Biomass Burning Aerosols during the 2007 San Diego Wildfires, Environ. Sci. Technol., 47, 7633–7643, https://doi.org/10.1021/es4004137, 2013.

Zaveri, R. A., Barnard, J., Easter, R., Riemer, N., and West, M.: Particle-resolved simulation of aerosol size, composition, mixing state, and the associated optical and cloud condensation nuclei activation properties in an evolving urban plume, J. Geophys. Res., 115, D17210, https://doi.org/10.1029/2009JD013616, 2010.

Zhang, G. H., Bi, X. H., Chan, L. Y., Li, L., Wang, X. M., Feng, J. L., Sheng, G. Y., Fu, J. M., Li, M., and Zhou, Z.: Enhanced trimethylamine-containing particles during fog events detected by single particle aerosol mass spectrometry in urban Guangzhou, China, Atmos. Environ., 55, 121–126, https://doi.org/10.1016/j.atmosenv.2012.03.038, 2012.

Zhang, G. H., Han, B. X., Bi, X. H., Dai, S. X., Huang, W., Chen, D. H., Wang, X. M., Sheng, G. Y., Fu, J. M., and Zhou, Z.: Characteristics of individual particles in the atmosphere of Guangzhou by single particle mass spectrometry, Atmos. Res., 153, 286–295, https://doi.org/10.1016/j.atmosres.2014.08.016, 2015.

Zhang, J. K., Luo, B., Zhang, J. Q., Ouyang, F., Song, H. Y., Liu, P. C., Cao, P., Schäfer, K., Wang, S. G., Huang, X. J., and Lin, Y. F.: Analysis of the characteristics of single atmospheric particles in Chengdu using single particle mass spectrometry, Atmos. Environ., 157, 91–100, https://doi.org/10.1016/j.atmosenv.2017.03.012, 2017a.

Zhang, G. H., Lin, Q. H., Peng, L., Yang, Y. X., Fu, Y. Z., Bi, X. H., Li, M., Chen, D. H., Chen, J. X., Cai, Z., Wang, X. M., Peng, P. A., Sheng, G. Y., Zhou, Z.: Insight into the in-cloud formation of oxalate based on in situ measurement by single particle mass spectrometry, Atmos. Chem. Phys., 17 (22), 13891–13901, https://doi.org/10.5194/acp-17-13891-2017, 2017b.

Zhang, G. H., Han, B. X., Bi, X. H., Dai, S. X., Huang, W., Chen, D. H., Wang, X. M., Sheng, G. Y., Fu, J. M., and Zhou, Z.: Characteristics of individual particles in the atmosphere of Guangzhou by single particle mass spectrometry, Atmos. Res., 153, 286–295, https://dx.doi.org/10.1016/j.atmosres.2014.08.016, 2015.

Zhang, G. H., Lian, X. F., Fu, Y. Z., Lin, Q. H., Li, L., Song, W., Wang, Z. Y., Tang, M. J., Chen, D. H., Bi, X. H., Wang, X. M., and Sheng, G. Y.: High secondary formation of nitrogen-containing organics

847   (NOCs) and its possible link to oxidized organics and ammonium, Atmos. Chem. Phys., 20,
848   1469–1481, https://doi.org/10.5194/acp-20-1469-2020, 2020.

849 Zhang, X. H., Xu, J. Z., Kang, S. C., Zhang, Q., and Sun, J. Y.: Chemical characterization and sources of
850   submicron aerosols in the northeastern Qinghai–Tibet Plateau: insights from high-resolution mass
851   spectrometry, Atmos. Chem. Phys., 19, 7897−7911, https://doi.org/10.5194/acp-19-7897-2019, 2019a.

852 Zhang, G. H., Lin, Q. H., Peng, L., Yang, Y. X., Jiang, F., Liu, F. X., Song, W., Chen, D. H., Cai, Z., Bi, X.
853   H., Miller, M., Tang, M. J., Huang, W. L., Wang, X. M., Peng, P. A., Shen, G. Y.: Oxalate Formation
854   Enhanced by Fe-Containing Particles and Environmental Implications, Environ. Sci. Technol., 53,
855   1269–1277, https://doi.org/10.1021/acs.est.8b05280, 2019b.

856 Zhang, N. N., Cao, J. J., Xu, H. M., and Zhu, C. S.: Elemental compositions of $PM_{2.5}$ and TSP in Lijiang,
857   southeastern edge of Tibetan Plateau during pre-monsoon period, Particuology, 11(1), 63–69,
858   https://doi.org/10.1016/j.partic.2012.08.002, 2013.

859 Zhang, S. P., Xing, J., Sarwar, G., Ge, Y. L., He, H., Duan, F. K., Zhao, Y., He, K. B., Zhu, L. D., Chu, B.
860   W.: Parameterization of heterogeneous reaction of SO_2 to sulfate on dust with coexistence of NH_3 and
861   NO_2 under different humidity conditions, Atmos. Environ., 208, 133–140,
862   https://doi.org/10.1016/j.atmosenv.2019.04.004, 2019c.

863 Zhao, S. Y., Tie, X. X., Long, X., and Cao, J. J.: Impacts of Himalayas on black carbon over the Tibetan
864   Plateau during summer monsoon, Sci. Total Environ., 598, 307–318,
865   https://doi.org/10.1016/j.scitotenv.2017.04.101, 2017.

866

867 Table 1. The number concentrations, average percentages and characteristic ions of nine types
868 of particles during the entire campaign, and the average percentages of the major six particle
869 types during two episodes.

Type	Number count	Fraction in total (%)	Episode 1 (%)	Episode 2 (%)	Tracer ions
rich-K	151040	30.9	29.0	39.3	$^{39}K^+$, $^{26}CN^-$, $^{42}CNO^-$, $^{46}NO_2^-$, $^{62}NO_3^-$, $^{97}HSO_4^-$
BB	91322	18.7	11.5	14.2	$^{39}K^+$, levoglucosan ($^{45}CHO_2^-$, $^{59}C_2H_3O_2^-$, $^{71}C_3H_3O_2^-$, $^{73}C_3HO_3^-$), $^{26}CN^-$, $^{35,37}Cl^-$, $^{42}CNO^-$, $^{46}NO_2^-$, $^{62}NO_3^-$, $^{97}HSO_4^-$
OC	62446	12.8	8.1	10.0	$^{27}C_2H_3^+$, $^{37}C_3H^+$, $^{38}C_3H_2^+$, $^{39}K^+/C_3H_3^+$, $^{43}C_2H_3O^+$, $^{51}C_4H_3^+$, $^{26}CN^-$, $^{42}CNO^-$, $^{46}NO_2^-$, $^{62}NO_3^-$, $^{97}HSO_4^-$
Ammonium	58317	11.9	17.5	13.5	$^{12}C^+$, $^{18}NH_4^+$, $^{39}K^+$, $^{58}C_2H_5NHCH_2^+$, $^{97}HSO_4^-$, $^{195}H(HSO_4)_2^-$
EC-aged	53337	10.9	10.0	17.2	$C_n^\pm$ (n =1 ~ 5), $^{39}K^+$, $^{97}HSO_4^-$
Dust	52533	10.7	20.3	1.3	$^{40}Ca^+$, $^{56}CaO^+$, $^{16}O^-$, $^{17}OH^-$, $^{76}SiO_3^-$, $^{79}PO_3^-$
NaK-SN	13726	2.8	na	na	$^{23}Na^+$, $^{39}K^+$, $^{62}NO_3^-$, $^{97}HSO_4^-$
Metal	4672	1.0	na	na	$^{51}V^+$, $^{56}Fe^+$, $^{64,66,68}Zn^+$, $^{206,207,208}Pb^+$
Others	1580	0.3	na	na	No obvious characteristic peaks

870

Figure captions:

Figure 1. Box and whisker diurnal plots of the number concentration of the main particle types (a) rich-Potassium (K), (b) Biomass burning (BB), (c) Organic carbon (OC), (d) Ammonium, (e) Element carbon (EC)-aged, (f) Dust in hourly resolution. The lower, middle, and upper lines of the boxes denote the 25th, 50th, and 75th percentiles. The lower and upper whiskers represent the 10th and 90th percentiles, respectively. Average values are shown in white dots.

Figure 2. Maps of the mean HYSPLIT back trajectory clusters (72 h) at the height of 500 m during the whole field observation. Embedded pie chart represents the relative fraction of each particle type in the four clusters.

Figure 3. SPAMS-specific size distributions of the relative number fraction (%) of the total particles for nine groups during (a) the total sampling campaign and two episodes of (b) E1 and (c) E2.

Figure 4. Number fractions of secondary markers associated with the six particle types (rich-K, BB, OC, Ammonium, EC-aged, Dust) during the whole observation. Secondary species include sulfate ($^{97}HSO_4^-$), sulfuric acid ($^{195}H(HSO_4)_2^-$), nitrate ($^{62}NO_3^-$), ammonium ($^{18}NH_4^+$), amine ($^{58}C_2H_5NHCH_2^+$), and oxalate ($^{89}HC_2O_4^-$) ions.

Figure 5. Number fractions of secondary markers associated with the six particle types (i.e., rich-K, BB, OC, Ammonium, EC-aged, and Dust) in four clusters. Secondary species abbreviations as in Figure 4.

Figure 6. Correlations between the relative number fractions of the secondary species (a) $^{43}C_2H_3O^+$, (b) $^{89}HC_2O_4^-$, (c) $^{18}NH_4^+$, (d) $^{62}NO_3^-$, (e) $^{97}HSO_4^-$ and O_x concentration during E1 (blue square) and E2 (red dot).

Figure 7. Correlations between the relative number fractions of the secondary species (a) $^{43}C_2H_3O^+$, (b) $^{89}HC_2O_4^-$, (c) $^{18}NH_4^+$, (d) $^{62}NO_3^-$, (e) $^{97}HSO_4^-$ and relative humidity (RH) during E1 (cyan dot) and E2 (orange square).
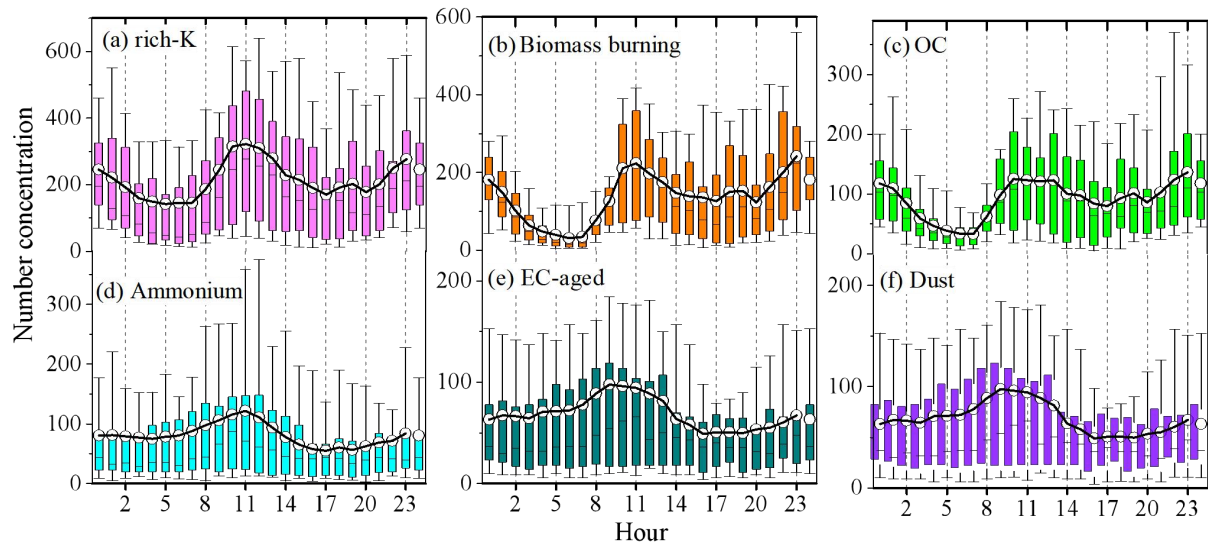
897

898 Figure 1. Box and whisker diurnal plots of the number concentration of the main particle types (a)

899 rich-Potassium (K), (b) Biomass burning (BB), (c) Organic carbon (OC), (d) Ammonium, (e) Element

900 carbon (EC)-aged, (f) Dust in hourly resolution. The lower, middle, and upper lines of the boxes denote the

901 25th, 50th, and 75th percentiles. The lower and upper whiskers represent the 10th and 90th percentiles,

902 respectively. Average values are shown in white dots.
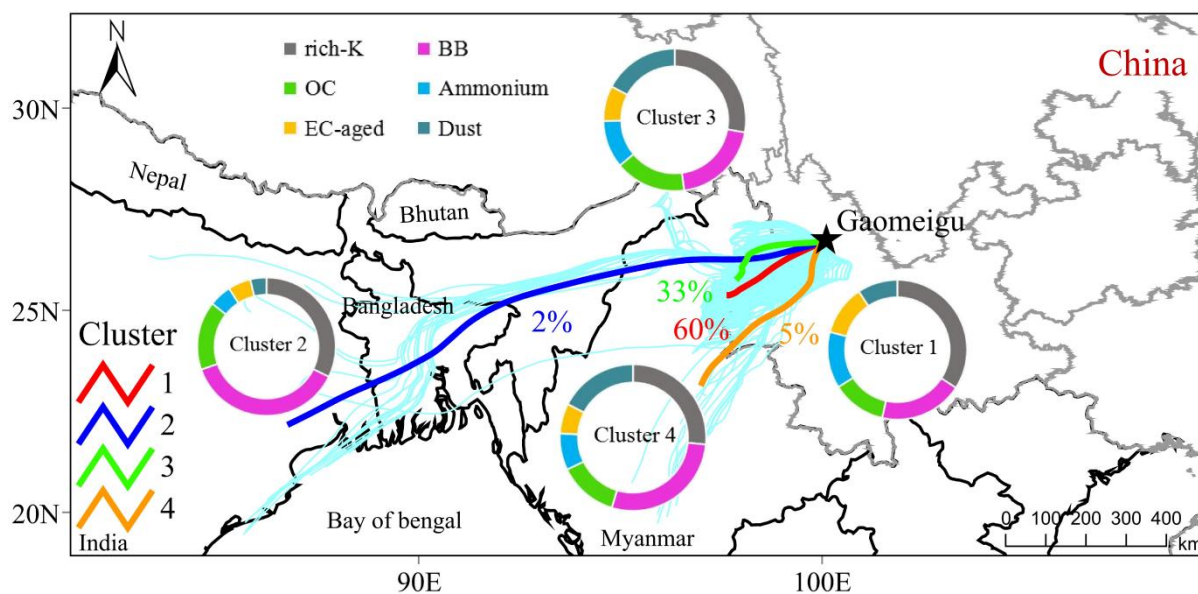
903

904 Figure 2. Maps of the mean HYSPLIT back trajectory clusters (72 h) at the height of 500 m during the

905 whole field observation. Embedded pie chart represents the relative fraction of each particle type in the

906 four clusters.
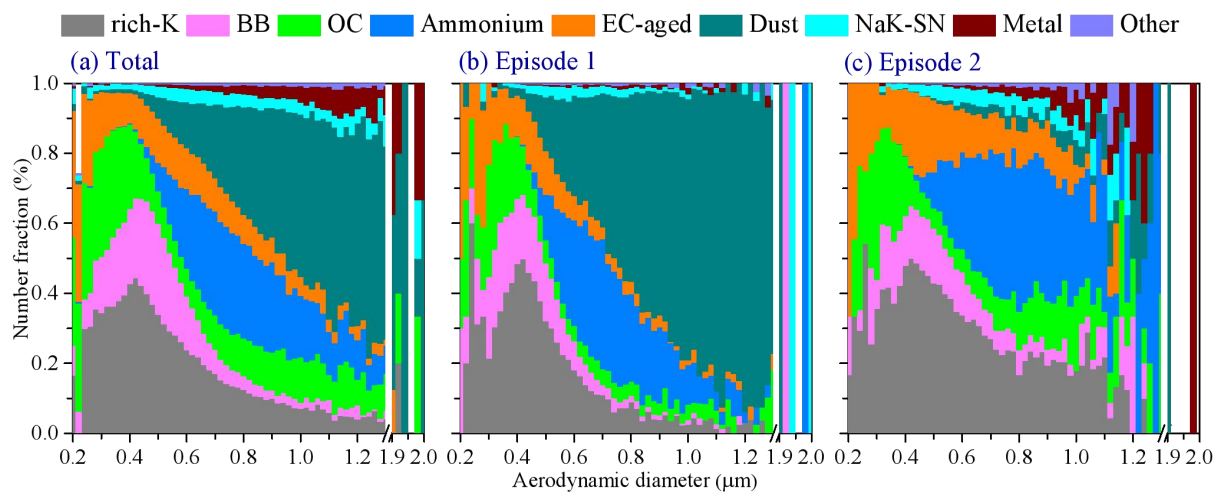
907

908 Figure 3. SPAMS-specific size distributions of the relative number fraction (%) of the total particles for

909 nine groups during (a) the total sampling campaign and two episodes of (b) E1 and (c) E2.
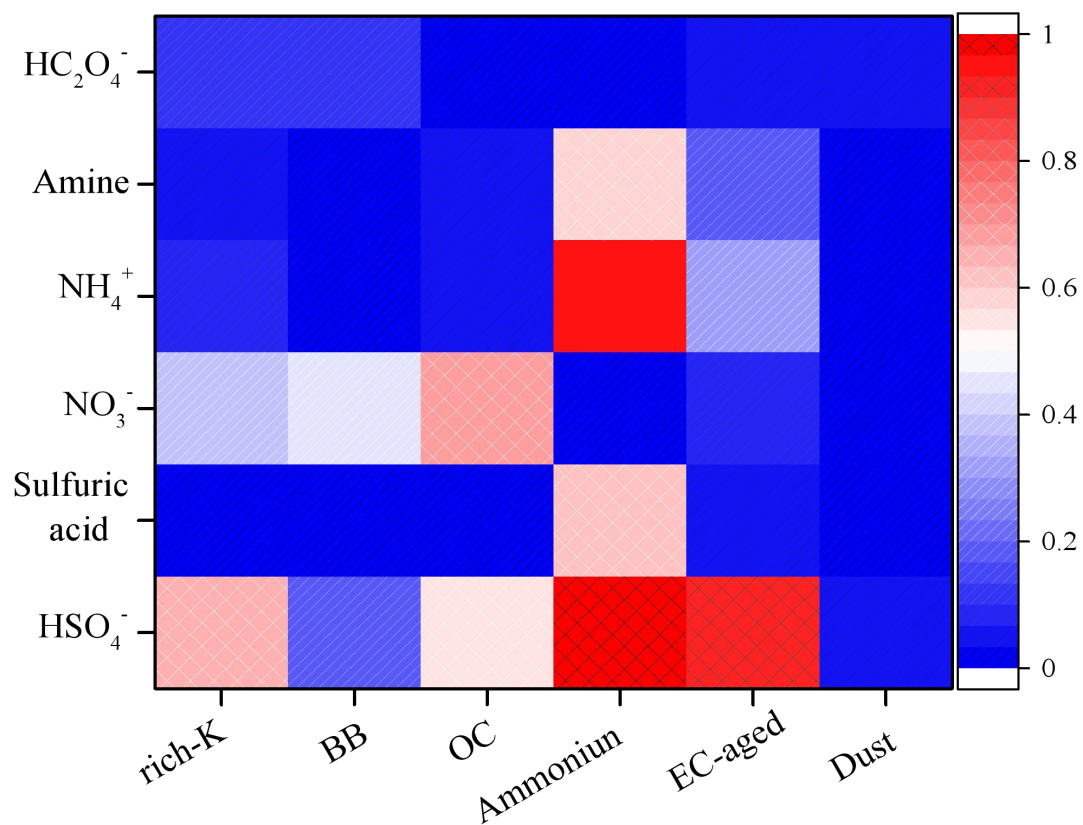
910

911   Figure 4. Number fractions of secondary markers associated with the six particle types (rich-K, BB, OC,

912   Ammonium, EC-aged, Dust) during the whole observation. Secondary species include sulfate ($^{97}HSO_4^-$),

913   sulfuric acid ($^{195}H(HSO_4)_2^-$), nitrate ($^{62}NO_3^-$), ammonium ($^{18}NH_4^+$), amine ($^{58}C_2H_5NHCH_2^+$), and oxalate

914   ($^{89}HC_2O_4^-$) ions.

915
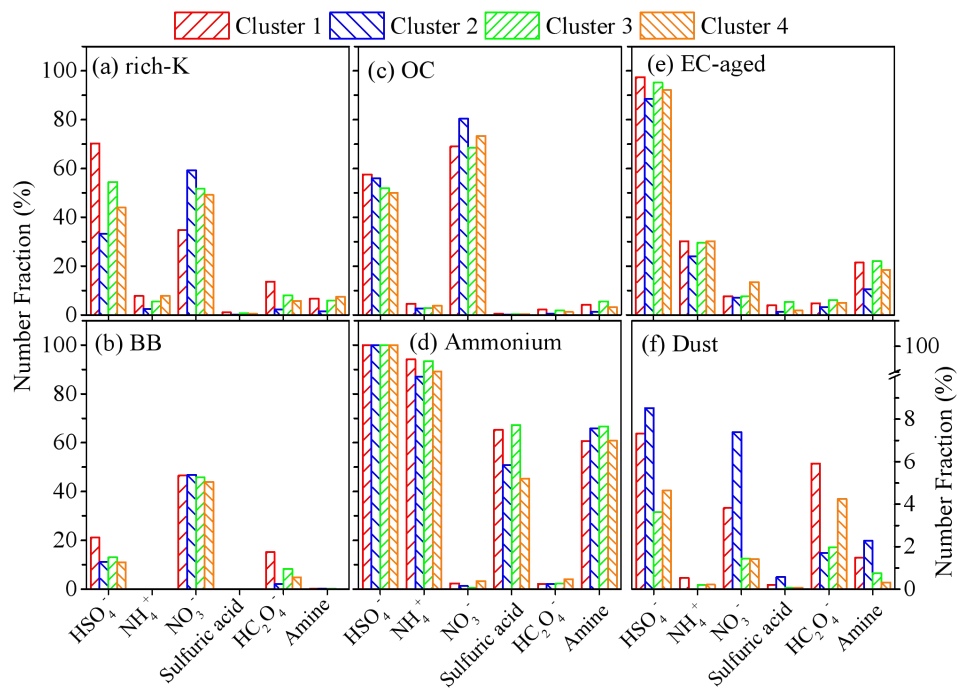
916

917 Figure 5. Number fractions of secondary markers associated with the six particle types (i.e., rich-K, BB,

918 OC, Ammonium, EC-aged, and Dust) in four clusters. Secondary species abbreviations as in Figure 4.

919
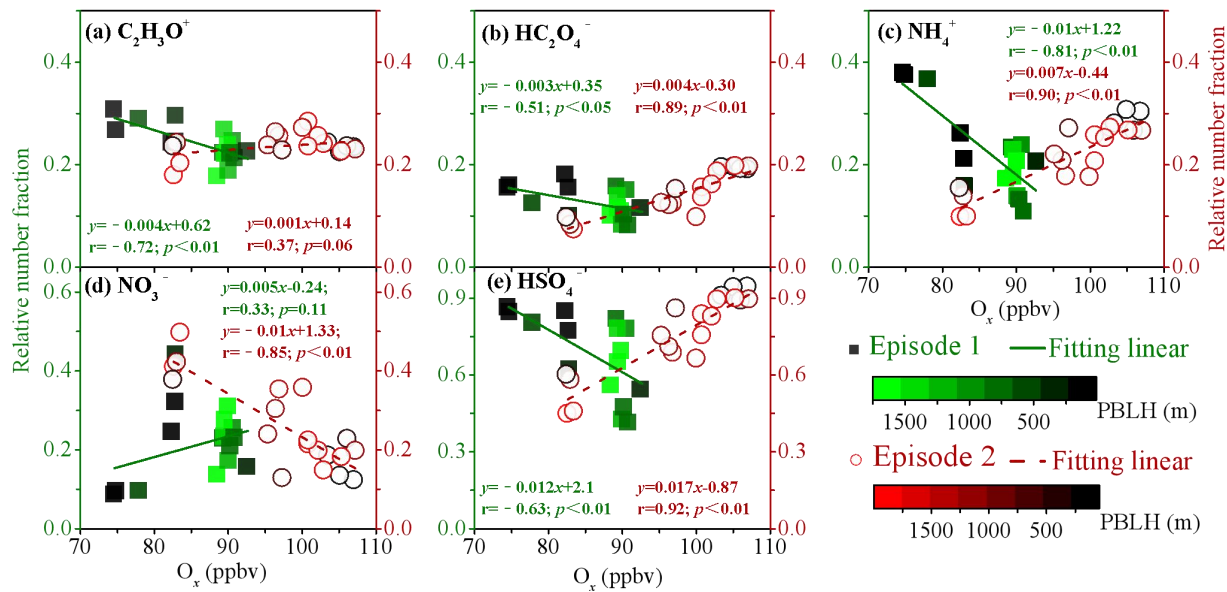
921 Figure 6. Correlations between the relative number fractions of the secondary species (a) $^{43}C_2H_3O^+$, (b)
922 $^{89}HC_2O_4^-$, (c) $^{18}NH_4^+$, (d) $^{62}NO_3^-$, (e) $^{97}HSO_4^-$ and O_x concentration during E1 (blue square) and E2 (red
923 dot).
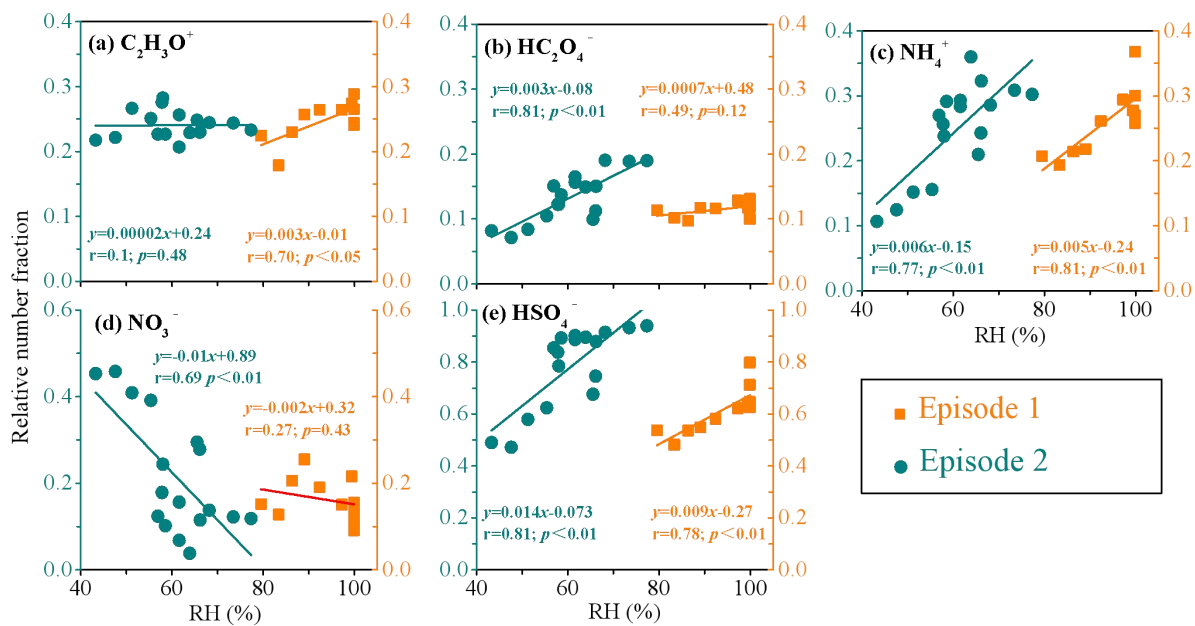
924

925 Figure 7. Correlations between the relative number fractions of the secondary species (a) $^{43}C_2H_3O^+$, (b)

926 $^{89}HC_2O_4^-$, (c) $^{18}NH_4^+$, (d) $^{62}NO_3^-$, (e) $^{97}HSO_4^-$ and relative humidity (RH) during E1 (cyan dot) and E2

927 (orange square).

928